Scattering from Breaking Gravity Waves Without Wind

P. H. Y. Lee, J. D. Barter, K. L. Beach, B. M. Lake, H. Rungaldier, H. R. Thompson, Jr., and R. Yee

***Abstract*—Scattering experiments from breaking gravity waves conducted at a wave tank facility at small grazing angles in the absence of wind are analyzed. Breaking gravity waves are studied using a fully plane polarimetric horizontal (HH), vertical (VV), vertically transmitted and horizontally received polarization (VH), and horizontally transmitted and vertically received polarization (HV) pulse-chirped X-band radar in conjunction with optical instruments: the plane polarimetric optical specular event detector (OSED) and side-looking camera (SLC). Spatially and temporally resolved radar backscatter has been measured and temporally correlated to the data obtained from the optical diagnostics. The experiments yield the following results: 1) enhanced scattering compared to Bragg scattering levels occurs throughout the evolutionary process of wave-breaking, i.e., the radar scatters strongly from both the unbroken and broken surfaces; 2) an explanation is found for the observation that the scatterer Doppler frequency is slightly less than the Doppler frequency corresponding to the fundamental wave phase speed; 3) a representative non-Bragg cross section of a breaking wave can be obtained; and 4) a breaking wave surface is found to be an efficient depolarizer.**

***Index Terms*—Sea surface electromagnetic scattering.**

I. Introduction

ANALYSIS of ocean scattering data at microwave frequencies has indicated that the ubiquitous presence of fast scatterers and super events provides compelling evidence of non-Bragg scattering processes [1]–[3]. At small grazing angles, the fact that fast scatterers provided the main contribution to the returns for the horizontal polarization underscored the importance of non-Bragg scattering. The experimental evidence pointed to incipient or actively breaking water waves as the source of fast scatterers and it was conjectured that the surface geometry of a breaking wave contained scattering elements, that could provide not only specular-like reflection from curved water facets, but also multiple scattering, which may or may not include a reflection at the Brewster angle. The experimental verification of these conjectures made use of a polarimetric optical imaging instrument [optical specular event detector (OSED)] operated in conjunction with the microwave scatterometer. Temporal correlations of the OSED images with the temporal radar data yielded direct verification of the conjectures regarding the scattering mechanisms giving rise to fast scatterers and super events [4]. Thus, the important role of breaking waves in scattering from water surfaces has been established by experiment.

Several important phenomenological results obtained from experimental observations of X-band (8.5–9.6 GHz) scattering from mechanically generated breaking waves at small grazing angles (4.5–11°) have been shown in previous reports [5]–[7]. The main points are the following: 1) breaking waves provide the major contribution to the fast scatterer cross section; 2) breaking waves are the major source of depolarized returns; 3) breaking waves yield Lorentzian and Voigtian lineshapes in time-averaged Doppler spectra; and 4) a small amount of "slow," Bragg scatterers (with Gaussian power spectral density (PSD) lineshapes) are also generated as the wave breaks and are detectable after the breaking wave decays. In order to understand the issue at a deeper level, however, we need to answer several questions regarding the backscatter from a breaking wave surface. 1) Where on the breaking-wave surface does scattering occur? 2) Why is the measured PSD peak frequency less than the Doppler frequency which corresponds to the phase speed of the gravity wave? 3) What is the non-Bragg cross section of a breaking wave? The present experiments have been conducted with these questions in mind. The reason to pursue the investigation along these lines is that ultimately, one must understand the physical mechanism which governs the backscatter from breaking wave surfaces so that useful input may be provided for modeling purposes.

The X-band pulse-chirped radar (PCR) which was the principal instrument in this experiment and the experimental facility have been reported elsewhere [8]. Details of the OSED have been described in [4]. The PCR can be operated in two different modes, the nonrange-resolved mode and the range-resolved mode. In the former mode, the system operates as a single frequency radar in which any number of the 32 transmitted frequencies can be used simultaneously and independently, and the range resolution is governed by the coarse range attenuation gate of $\sim$4 m. In the latter mode, 32 range gates are available with range resolution of 13.6 cm. Using the PCR in each mode, we conducted an investigation of small-grazing-angle microwave backscattering from breaking waves, in the absence of wind. In the discussion to follow, we will first describe the experimental configuration and review the visual observations made on the evolution of

Manuscript received April 14, 1997; revised September 23, 1997. This work was supported by the Advanced Sensors Application Program in the Intelligence Systems Support Office, Department of Defense, contract DMA 800-94-C-6008.

The authors are with TRW Space & Electronics, Redondo Beach, CA 90278.

Publisher Item Identifier S 0018-926X(98)01046-1.

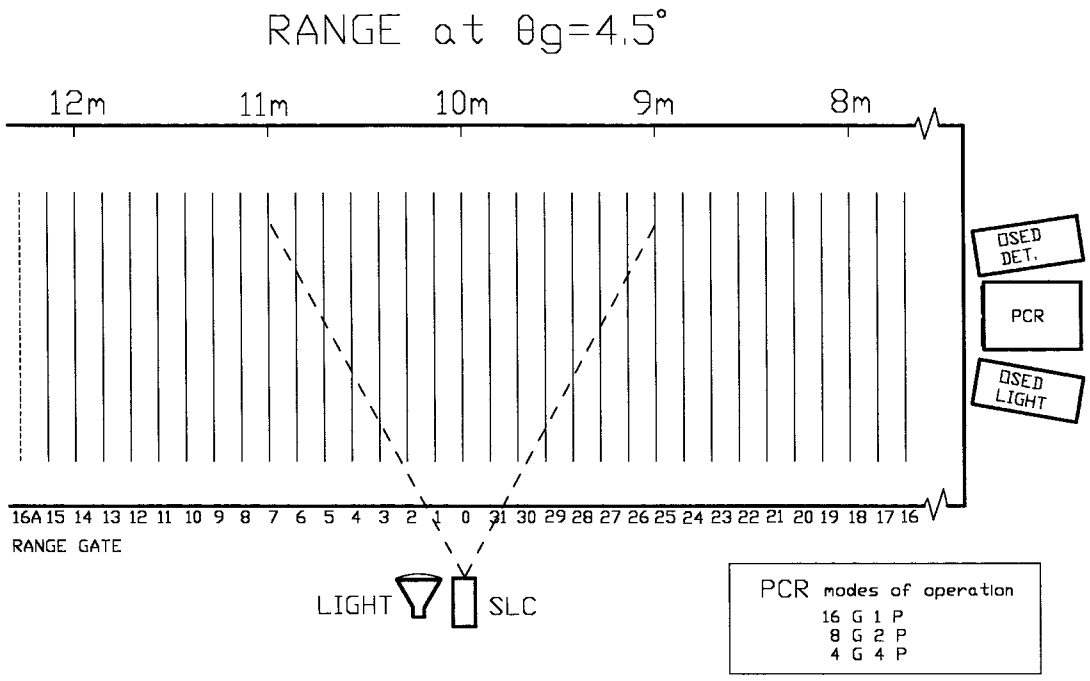

Fig. 1. The correspondence of the 32 range gates to the PCR line-of-sight range. Note the folded scheme of the gate numbering. Beyond the principal gates, the same gate pattern (with the same gate numbering) is repeated and are called aliased gates (e.g., gate 16a is the alias of gate 16, which is further in range than gate 15). When the PCR is operated in the 16G1P mode (that is, 16 gates and one polarization element stored for off-line analysis), any 16 gates and any polarization may be chosen. In the paper, the 16G1P mode comprises the odd-numbered gates and horizontal (HH) polarization. The 8G2P mode comprises every second odd gate starting with gate one and HH and vertical (VV) polarizations. The 4G4P mode comprises the gates 31, 30, 29, and 28 and all four elements in the polarization matrix horizontal (HH), vertical (VV), vertically transmitted and horizontally received polarization (VH), and horizontally transmitted and vertically received polarization.

breaking waves [9]. Specific examples of time and range-resolved breaking wave RCS which are correlated with the resulting images obtained from the optical diagnostics will then be shown, followed by the range-resolved grazing-angle-dependent Doppler spectra. These data contain the information with which we will answer, among other questions, those raised in the previous paragraph.

II. Experiments and Results

A. Experimental Configuration at UCSB/OEL

The wavetank at UCSB/OEL is 53 m long, 4.3 m wide and 2.1 m deep with a computer controlled plunging type wavemaker at the end opposite the test section [8]. Fig. 1 shows a schematic of the 32 range gates relative to the radar range. A folded scheme has been adopted for the gate assignment such that the range gate zero, which contains the radar boresight, is set at 10-m range. In the present configuration, the radar boresight grazing angles may be set to any value within the range of 4.5°–11°. Grazing angles are reported for range gate zero at 10-m boresight range. The principal gates are thus 16–31 for gates closer to the radar and gates 0–15 for gates further from the radar. The same gate pattern is repeated for gates closer than principal gate 16, or gates further than principal gate 15 and are called the "aliased" gates. In short, since the 32 range-gate pattern repeats itself, an aliased gate is always 32 gates (or 4.35 m) away from the principal gate of the same gate number. Returns from aliased gates are progressively attenuated by the coarse range attenuators. A side-looking-camera is situated at approximately gate zero with a field of view which is indicated by the dashed lines emanating from the SLC in the figure (approximately gates 7–24). The OSED and the SLC each have their separate light sources. It should be pointed out that although both visible diagnostics may be operated simultaneously, the SLC light source must be turned off for the OSED to operate in a polarimetrically calibrated mode. Synchronization of the PCR, the OSED and the SLC is accomplished by the incorporation of appropriate forms of a global positioning system (GPS) master clock output into the data streams of each detector. The instruments are temporally synchronized to within 1 ms, which is more than adequate for the hydrodynamic time scales of interest. In the range-resolved mode, the PCR may operate in one of the following data collection modes: 16 gates at one polarization (16G1P), eight gates at two polarizations (8G2P) or four gates at four polarizations (4G4P). In all cases, the range gate Fourier transform is performed on the complete set of data from 32 frequencies to yield RCS at 32 range gates, but only the specified data are stored for off-line analysis. RCS data are available each millisecond either in range resolved or nonrange resolved modes. PSD spectra at each range gate are available every second at reduced frequency resolution. Details of the range gate transform are given in [8, Appendix E].

For the present paper, mechanically generated breaking gravity waves are used. The 3- or 4-m gravity waves are generated with sideband modulation and it is the growth of the sideband-modulated instability [10] that causes the waves

TABLE I
THE CONDITIONS DESCRIBING THE SIDEBAND-MODULATED GRAVITY WAVES (SEE TEXT FOR NOTATION)

λ_W (m)	f_o (Hz)	f_+ (Hz)	f_- (Hz)	a_s/a_o	ka
4.0	0.624	0.704	0.544	0.3	0.165
3.0	0.721	0.903	0.539	0.003	0.28

to break at the appropriate location in the wavetank, which we call the test section (i.e., the location of the radar footprint). The essential conditions describing the sideband-modulated gravity waves are listed in Table I where λ_W and f_o denote the wavelength and frequency of the fundamental gravity wave, respectively, f_+ and f_- denote the upper and lower sideband frequencies, respectively, a_s/a_o is the sideband amplitude to fundamental amplitude at generation (the upper and lower sideband amplitudes are equal), and ka is the characteristic wave slope with $k = 2\pi/\lambda_w$ and $a^2 = a_o^2 + 2a_s^2$.

For a fixed ka, one may conveniently control the "degree" of breaking by varying a_s/a_o. Scattering from waves in which the degree of breaking is "incipient," "mild," "intermediate," or "full," depending on how energetic the breaking process is observed to be has been described elsewhere [5]. In this paper, only fully breaking waves with the conditions described in Table I are considered.

The stages through which the breaking wave evolves are summarized in cartoon form in Fig. 2. A more detailed description of the evolution of sideband-modulated breaking gravity waves is given in the report, "Profiles of breaking gravity waves," in which the terminology of steepening, cresting, involution, jetting, splashing, foaming, shedding, and decay was adopted [9]. Two examples of breaking-wave profiles are shown in Fig. 3. In the top figure, a steepened profile but with an unbroken surface is shown; in the bottom figure, a splashing or foaming stage with a broken surface is shown. Note that a wave-breaking sequence may commence or terminate at a range outside the range of principal gates since the range at which a wave begins to break can be only approximately controlled. This situation poses no problem since the radar and the OSED (which view the same scene at the same grazing angle) can together accurately locate the correct gate by means of the temporal and spatial fiducials obtained by calibration. In the following discussion, a recorded event outside of the principal gates will be designated as appearing in an aliased gate.

B. Temporal-Correlation of Radar Cross Sections (RCS) with SLC Images

Typical wave-breaking sequences of 3- and 4-m waves showing the temporal RCS record have been compared to the corresponding side-looking camera (SLC) camera images. The full set of RCS traces and their corresponding optical images are available in a separate report [11] but are not shown here for brevity. The results clearly reveal that *the broken wave surface contributes to the backscatter for a longer period of time than the unbroken surface*.

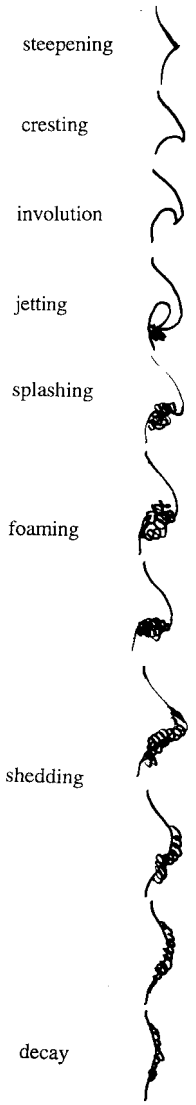

Fig. 2. A wave-profile sketch representation of the various stages of evolution of a breaking wave. See text (and especially [9]) for further details.

C. Temporal-Correlation of Radar Cross Sections with OSED Images

1) An Example of PCR Operation with 4-m Breaking Waves: Next, we show the correlation of RCS signals with OSED images. In this case, a 4-m breaking wave is examined. The PCR is operated in the 16G1P data archive mode with every odd-numbered gate selected and HH polarization selected. Fig. 4 shows the RCS record. The vertical scale denotes relative cross section where 54 dB corresponds to the RCS of 9×10^{-4} m^2 at 10-m range determined by scattering from a 1-in sphere (*in situ* calibrations will be discussed in Section II-F.). The range cell is $\sim$1 m in azimuth and 13.6 cm in range, thus the area of the range cell is 0.136 m^2. Characteristic wave profiles at the times corresponding to their appearance in the various gates are depicted by sketches along the top of the figure as derived from OSED images as presented in [11]. The wave-breaking commences at gate 11, progresses through the stages of evolution and decays at "aliased" gate 15 (i.e., gate

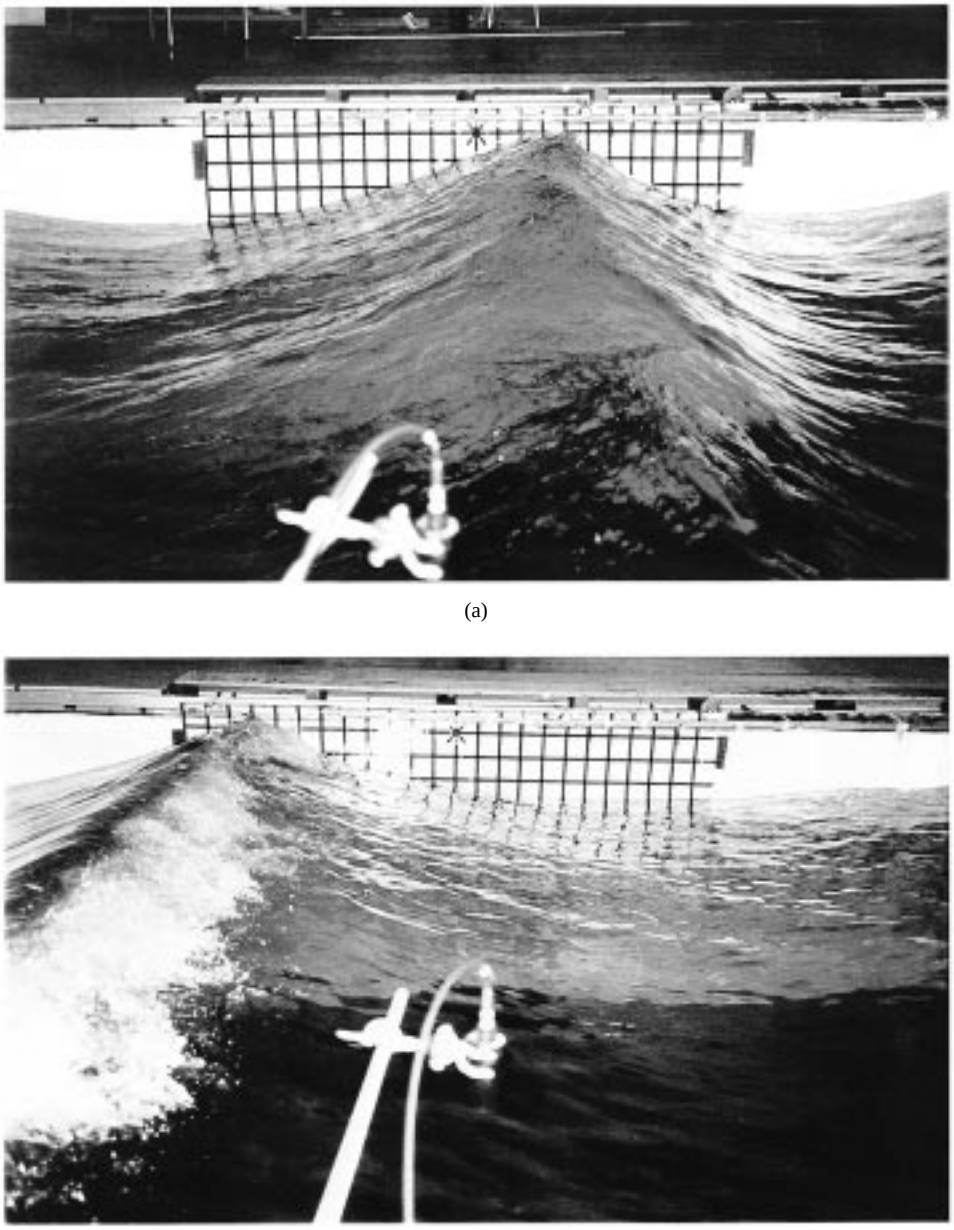

(a)

(b)

Fig. 3. Images of breaking wave surfaces. (a) A side view of a breaking wave at an early stage of evolution where the surface contains large slope but is unbroken. (b) A side view of a breaking wave at the "mid-life" stage of evolution where the surface is broken. The grids on the far wall have the dimension 0.1 × 0.1 m. It is easily seen that the broken wave surface fills the range cell of the radar (whose resolution is 1 m in azimuth and 0.136 m in range).

15a). As the wave breaks, patches of small scale roughness are "shed" from the gravity wave and become detectable by Bragg scatter after the wave has decayed (note the sequence of signals after $t = 254\,255$ s). Note that for this particular breaking wave, the Bragg scattering has a radar cross section which is ∼30 dB less than the radar cross section of a breaking wave surface. Post-break Bragg scattering is further discussed in the next section.

2) An Example of PCR Operation with 3-m Breaking Waves: In this example, we show the case of a 3-m breaking wave where the PCR is operated in the 8G2P mode with HH and VV of every fourth gate selected. The RCS record is shown in Fig. 5. The vertical scale denotes relative cross section where 54 dB corresponds to the RCS of a 1-in sphere at 10-m range. The range cell is ∼1 m in azimuth and 13.6 cm in range, thus, the area of the range cell is 0.136 m^2. Wave-breaking sketches corresponding to the various gates are also given across the top of this figure. Comparing the HH and VV signals at each individual gate, one notes that during the wave breaking process, the scatterers yield super events (i.e., HH $>$ VV) with only rare exceptions, as is evident from inspection of the RCS at gates 17a (i.e., aliased gate 17), 13, 9, 5, 1, and 29. At gate 25, one has HH $\approx$ VV, which is specular-like and supplies the exception to prove the rule. After a broken wave has decayed, small scale slower scatterers are observed (in SLC optical images) to be shed from the gravity wave giving rise to Bragg scattering [9], as manifested by the observation that VV $>$ HH. This is seen

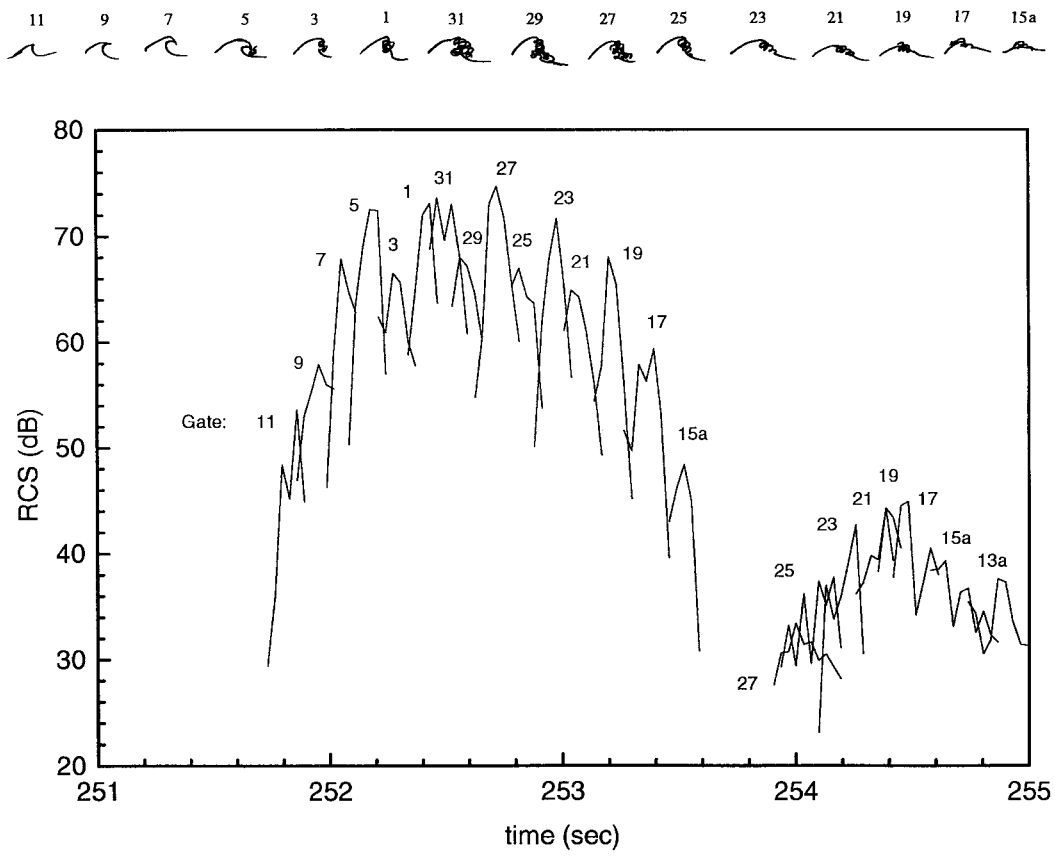

Fig. 4. The temporal RCS record of a typical wave-breaking sequence of a 4-m wave. Gate numbers are indicated above each HH RCS peak response. The vertical scale is relative, where 54 dB is equivalent to 9×10^{-4} m^2 radar scattering cross section, at 10-m range. For this sequence, the characteristic wave profiles at the various stages of evolution corresponding to their appearance in the various gates are depicted by sketches along the top of the figure. See text for description.

in the RCS of gates 5, 1, 29, 25 and 21. Note also that the gates 5, 1, and 29 with VV $>$ HH are at greater range than gate 25 at which the OSED observes the last broken surface return. Again, the small-scale structures are Bragg scatterers, which have been left behind ("shed") by the decaying crest. It will also be shown in the time-integrated Doppler spectra that the post-break Bragg scatterers are strongly influenced by the orbital motion of the gravity wave. The temporally and spatially corresponding OSED images are available in [11], but are not shown here for brevity.

3) Correlations: Quantitative correlations between the PCR and the OSED for the wave-breaking record of Fig. 5 are shown in Fig. 6. In Fig. 6(a) the peak temporal HH and VV relative cross sections (where 54 dB is the RCS of a 1-in sphere at 10 m) at each range are plotted against time. One notes that during the evolution of the wave-breaking process, the backscatter yields exclusively super events with HH $>$ VV. As the wave decays and small scale scatterers are shed, Bragg scatter again dominates and VV becomes greater than HH. Fig. 6(b) and (c) shows the temporal correlations between visible and microwave responses for the s-HH, and p-VV pairs, respectively (see [4] for further discussion). Fig. 6(d) shows the temporal correlation of the visible and microwave polarization ratios. Here we note that during the process of wave-breaking the polarization ratio correlates well. The visible polarization ratio becomes meaningless and is suppressed when the surface has only small scale disturbances and Bragg scattering dominates, since Bragg waves which are resonant at microwavelengths are not resonant at visible wavelengths and the OSED signal becomes dominated by noise. In summary, the correlation between PCR and OSED is found to be good for both scattering cross section and polarization ratio during spiking events when the OSED sees significant returns.

D. Scatterer Speed

From the time-resolved measurements of the RCS of breaking waves, one can estimate the scatterer speed. When scattering occurs through the Bragg mechanism, the scatterer speed is typically of the order of the phase speed of the Bragg-resonant wave (plus the orbital speed of the underlying gravity wave, if applicable) for free Bragg waves, or the phase speed of the gravity wave for bound Bragg waves. For non-Bragg scattering (which is readily distinguishable from Bragg scattering through the magnitude of the polarization ratio HH/VV), the scatterer speed is typically of the order of the phase speed of the gravity wave, which produces the backscatter. For our present situation, since the breaking gravity wave is evolving while it propagates through the range gates, the scatterer speed may be simply obtained by dividing the known gate-separation distances by the measured time intervals between peak gate responses, i.e., a "time-of-flight"

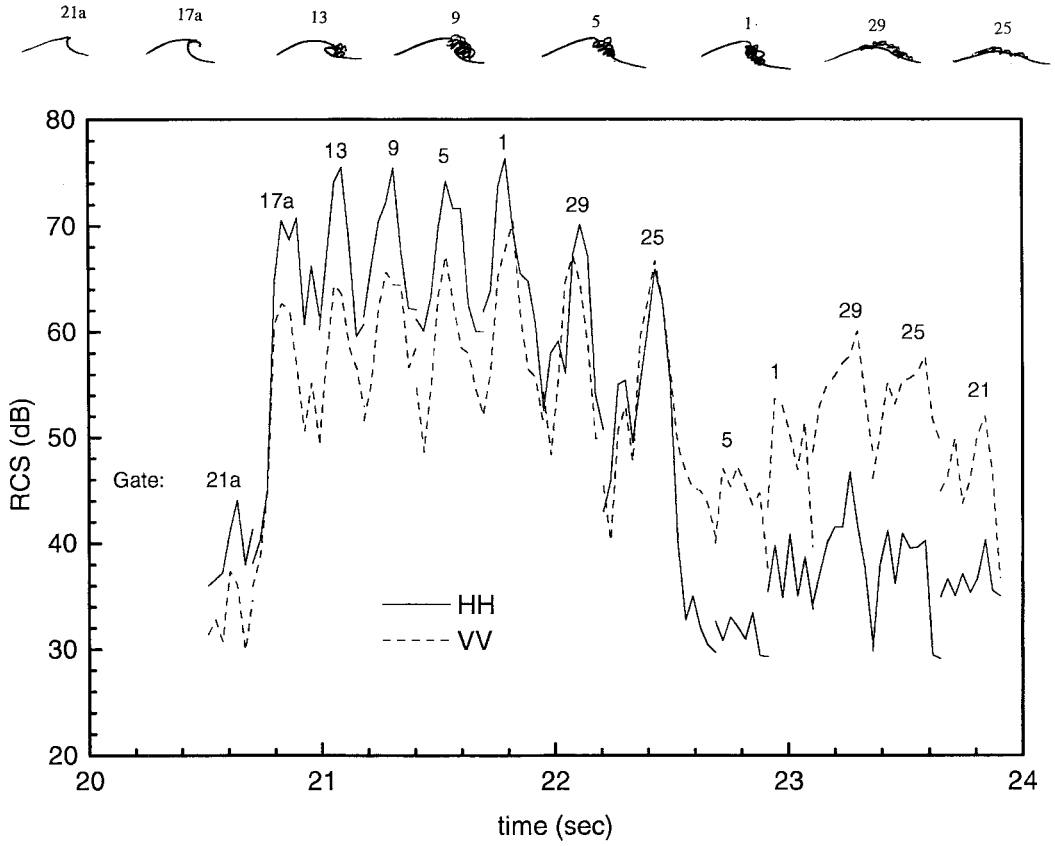

Fig. 5. The temporal RCS record of a typical wave-breaking sequence of a 3-m wave. The PCR is operated in the 8G2P mode where every fourth gate is selected and HH and VV are selected. Gate numbers are indicated above each HH (solid line) and VV (dashed line) RCS peak response. The vertical scale is relative, where 54 dB is equivalent to 9×10^{-4} m^2 radar scattering cross section, at 10-m range. For this sequence, the characteristic wave profiles at the various stages of evolution corresponding to their appearance in the various gates are depicted by wave-profile sketches along the top of the figure. Note that during the wave breaking process, the scatterers yield exclusively super events (HH $>$ VV). After a broken wave has decayed, small scale, slower scatterers yield Bragg scattering for which VV $>$ HH.

method. Another direct measurement of this effect might be obtained from time-resolved Doppler spectra. However, due to the requirements of the range calculation and the data rate limits of the PCR, the time resolution of Doppler spectra is insufficient to resolve an approximately 2-s breaking event. The results of three separate examples of 3-m breaking waves are shown in Fig. 7. In the case of Fig. 7(a), one sees that in the early stages of wave breaking—the scatterer speed slightly exceeds the phase speed of a $\lambda_W = 3$-m gravity wave (calculated from $c_p = \sqrt{g\lambda_W/2\pi}$ where g is the gravitational acceleration, yielding 2.16 m/s). At later stages, however, the scatterer speed slows to values below the phase speed. Fig. 7(b) and (c) illustrates the same result for two other breaking events. Many other examples show the same trend, and a simple physics model of the process can be used to provide an explanation. For a wave to break, the speed at the crest of the wave must exceed the phase speed, which accounts for the early stage of the wave-breaking evolution (e.g., involution and jetting), but at later stages when foaming and crashing has occurred (i.e., after the wave surface is broken), the wave energy has gradually dissipated so that the water mass (which provides the backscatter) has slowed down. Accurate accounting of the details of these processes must be treated by hydrodynamics modeling and is beyond the scope of this paper.

Since the bulk of the backscatter from breaking waves is due to "broken" wave surfaces, and such surfaces consist of scatterers which on average have velocities slower than the phase speed explain why the observed time-integrated Doppler spectra exhibit PSD peaks at frequencies slightly lower than the Doppler frequency corresponding to the phase speed of the gravity wave. Data on Doppler spectra, which exhibit this effect, will be shown in the next section.

We note that the results stated above are only valid for the types of breaking waves, i.e., energetic breakers with wave conditions such as those described in Table I. For incipiently or mildly breaking waves typical of wind-wave conditions in a moderate ocean environment, the situation could be quite different. Laboratory experiments on wind waves in the absence and presence of gravity waves have also been performed. The first-order effect of the absence of wind is to greatly reduce the amount of Bragg scatterers. The energy of breaking (as well as the wavelength of the most-likely-to-break waves) is strongly dependent on wind speed and fetch. However, these results will be reported separately.

E. Grazing Angle Dependent Doppler Spectra and Polarization Ratios

Using the PCR in the 4G4P mode, we obtained Doppler spectra for four consecutive gates (31, 30, 29 and 28) at all

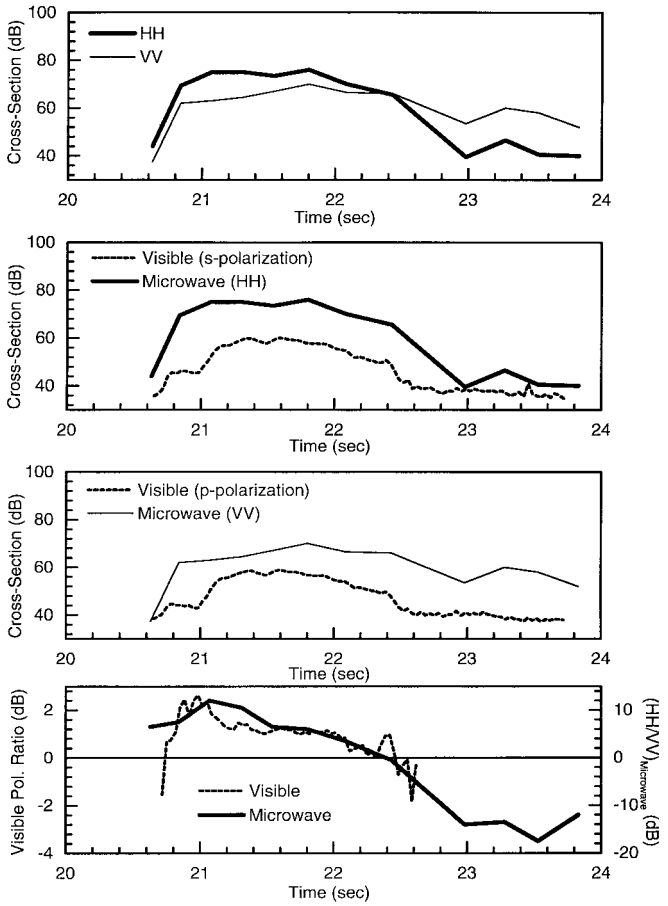

Fig. 6. (a) The temporal evolution of the HH and VV RCS for the case shown in Fig. 5. (b) Comparison of OSED s-polarization signal and PCR HH signal. (c) Comparison of OSED p-polarization signal and PCR VV signal. (d) Comparison of OSED s/p and PCR HH/VV polarization ratios.

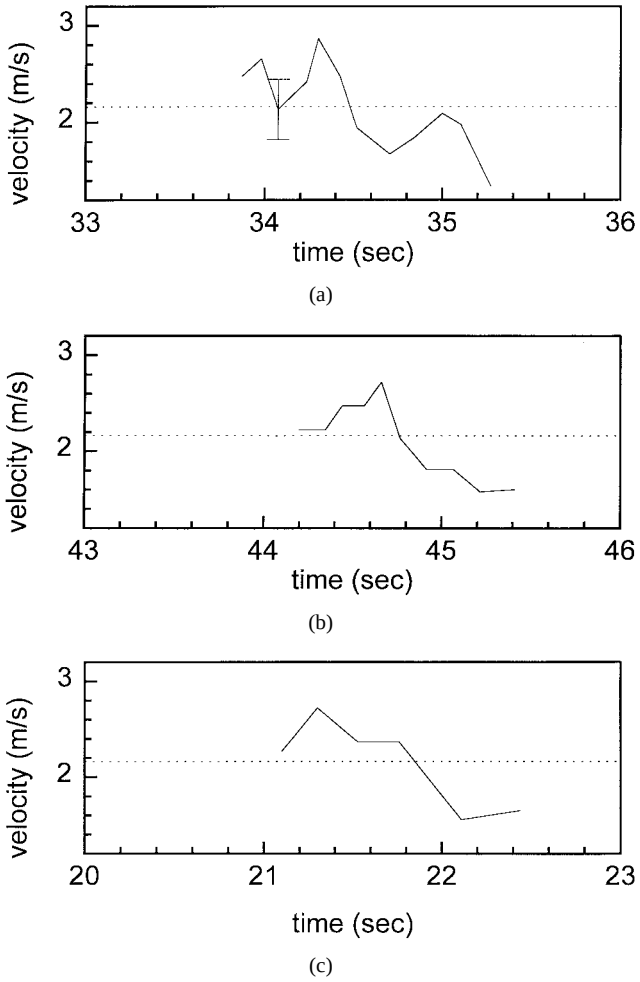

Fig. 7. Three examples of temporal records of scatterer speeds for the three different breaking sequences of sideband-modulated 3-m waves. A typical error bar, appropriate for all data points, is shown in the top figure.

polarizations (HH, VV, VH, and HV) for 4-m breaking waves. The Doppler spectra of gate 29, for grazing angle values of θ_g equals 4.5, 5.7, 6.8, 8, 9, 10, and 11°, respectively, have been analyzed and the full data set is found in [11]. Fig. 8(a)–(c) shows three examples at grazing angle values of 4.5, 8, and 11°. These Doppler spectra are obtained, from 4-m breaking waves, over a period of 409 s. These are familiar spectra which we have seen and reported before [5], [6]. Here we note, first of all, that for all cases, the peaks of the Doppler spectra are at frequencies roughly 10% less than the Doppler frequency corresponding to the phase speed of the gravity wave. This can readily be checked by noting that the Doppler frequency is given by

$$f_D = \frac{2\cos\theta_g}{\lambda}\, c_p \tag{1}$$

where λ is the microwave wavelength (taken to be 3.315 cm, which corresponds to the microwave frequency at the center of the chirp, 9.05 GHz), and c_p is the phase speed of the gravity wave which is 2.5 m/s for a 4-m wave. The values calculated from (1) yield $f_D = 150.4$ Hz, $f_D = 149.4$ Hz, and $f_D = 148$ Hz, for θ_g equals 4.5, 8, and 11°, respectively, whereas the measured Doppler spectra peak frequencies for the corresponding cases are seen to be lower than these values.

We next observe that as the grazing angle is increased, the post-breaking generation of Bragg scatterers not only becomes more visible in the VV polarization (below ~60 Hz), but also the frequency range of these Bragg scatterers is broader, extending into the range of negative frequencies. This too has been discussed before [7] and we briefly note here the explanation that as the grazing angle is increased, the radar "sees" more of the *trough* of the gravity wave (since less of the trough falls within the line-of-sight shadow at larger grazing angles), thus, more of the negative contribution of the orbital speed in the trough of the gravity wave is also seen. As a matter of fact, this shadowing effect is readily confirmed by visual observations (and SLC recordings) in which the OSED light source at the radar grazing angle demarcates the boundaries of light and shadow within the direct field-of-view of the PCR. Since the phase speed of the Bragg-resonant gravity-capillary wave is $c_{p(\mathrm{Bragg})} = 23$ cm/s at X-band, the Doppler frequency of free Bragg waves would be in the vicinity of 13–14 Hz. The broader spectral contribution due to Bragg scattering extending from about -10 Hz out to approximately 60 Hz in Fig. 8(c) indicates the strong contribution of the orbital velocity of the

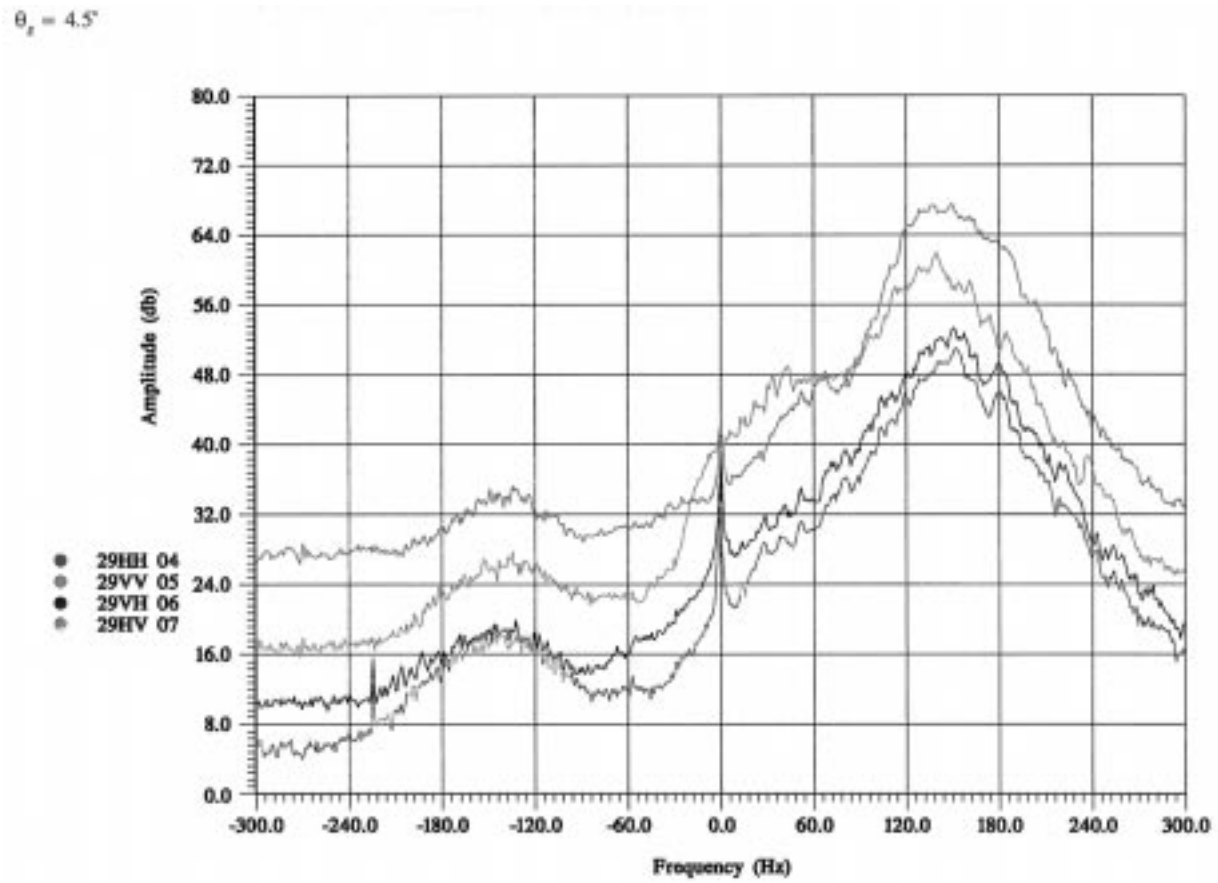

(a)

Fig. 8. Examples of Doppler spectra of 4-m sideband-modulated breaking waves. (a) Doppler spectra of HH, VV, VH, and HV from gate 29 at 4.5° grazing angle. Notice that for breaking waves only, the Doppler spectra clearly display the preponderance of super events, i.e., HH > VV. Note that as the grazing angle increases, the contribution of Bragg scattering (the portion of the PSD with Doppler frequencies below ∼60 Hz) also increases. This is due to small scale Bragg scatterers, which are detectable after a wave has broken. The fact that Bragg scatterers appear at both positive and negative Doppler frequencies indicates the effect of orbital motion due to the underlying gravity wave. Orbital motion yields a maximum positive radial velocity for the radar when the Bragg waves are on the crest of the gravity wave and a maximum negative orbital velocity for the radar when the Bragg waves are in the trough of the gravity wave.

underlying gravity wave. The maximum orbital speed may be estimated from $kac_p = 42$ cm/s where $ka = 0.28$ is taken from Table I and $c_p = 2.5$ m/s for a 4-m gravity wave. The maximum positive Doppler frequency of Bragg waves is thus $f_D = (2\cos\theta_g/\lambda)\,[kac_p + c_{p(\mathrm{Bragg})}] = 39.4$ Hz. The maximum negative Doppler frequency is due to the velocity difference between the Bragg wave phase speed and the maximum negative value of the orbital speed, i.e., $[-kac_p + c_{p(\mathrm{Bragg})}]$, which yields $f_D = -11.5$ Hz. If we also consider Bragg waves which are transitioning between bound and free states, then the contribution above ∼40 Hz may be accounted for. These values are in reasonably good agreement with observations.

The cross polarized components are prominent indicators of vigorous depolarization, as was noted and discussed in earlier reports [5]–[7]. The physical origin of depolarization is presently believed to be due to out-of-plane multiple scattering, or what Berry calls the anholonomic transport of polarization [12]. In the present set of data, we note that HV is consistently about 3 dB lower than VH. We suspect that this may be an indication of the limitations of the presently used *in situ* calibration. This will be addressed in upcoming comprehensive and absolute calibrations to be conducted in an anechoic chamber.

A plot of the breaking-wave cross section versus grazing angle is given in Fig. 9. The cross sections are estimated by the product of the peak PSD value of the Doppler spectrum and its −6 dB Doppler width

$$\sigma_{\mathrm{rel}} = 10\log\left(\mathrm{PSD}_{\mathrm{peak}} \cdot \Delta f_{-6\,\mathrm{dB}}\right) \tag{2}$$

and converted to units of m^2 using our *in situ* calibration with a 1-in sphere. The results are interesting in that for the limited range of grazing angles, the VV cross section is fairly flat, indicating that for the vertical polarization, the breaking wave surface is a rather isotropic scatterer. The HH and VH cross sections appear to have similar behavior with respect to grazing angle, exhibiting a broad peak near $\theta_g \sim 7°$, and falling off in value for $\theta_g \geq 9°$. If we examine polarization ratios, we note specifically that at $\theta_g = 4.5°$, we have HH/VV ≈ 7.5 dB, and HH/VH ≈ 15.5 dB. These values agree with earlier measurements and can be modeled using the anholonomic transport model with a statistical ensemble of double-bounce scatterers [6].

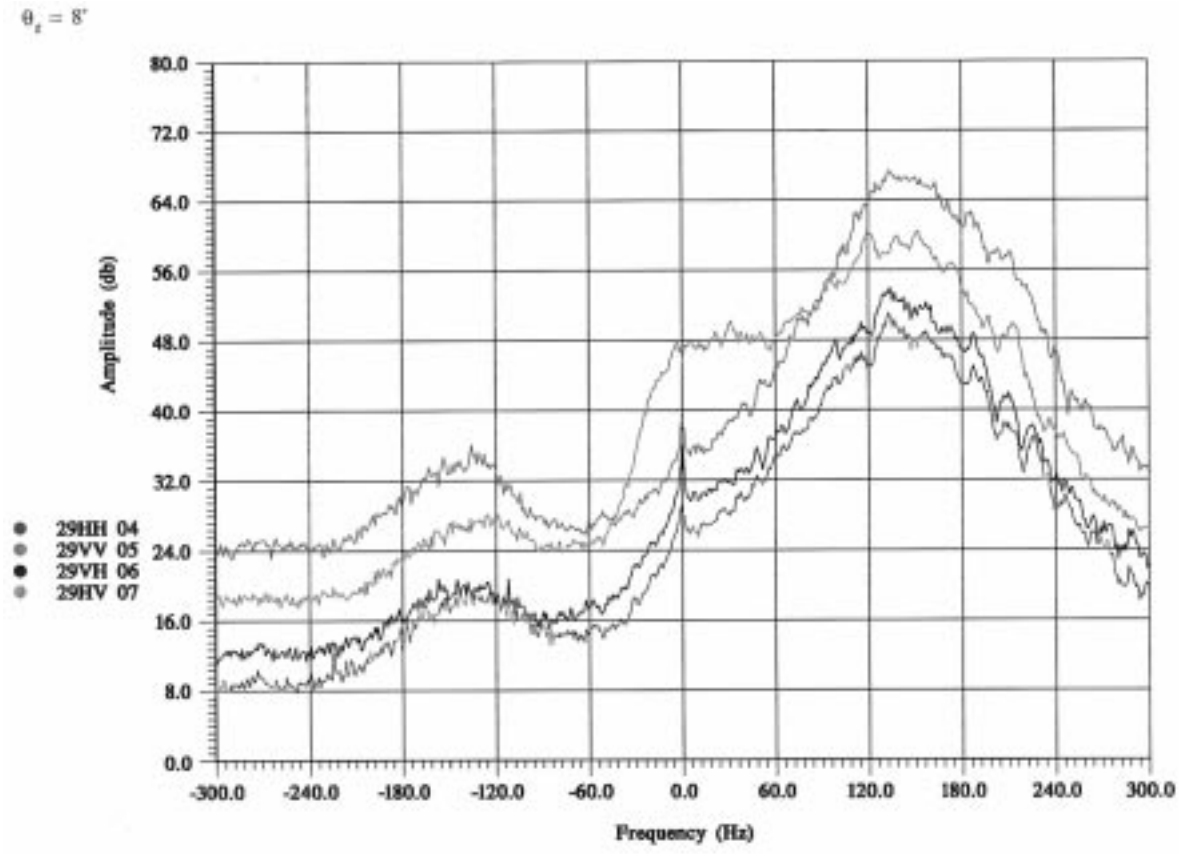

(b)

Fig. 8. (*Continued*.) Examples of Doppler spectra of 4-m sideband-modulated breaking waves. (b) Doppler spectra of HH, VV, VH, and HV from gate 29 at 8° grazing angle. Notice that for breaking waves only, the Doppler spectra clearly display the preponderance of super events, i.e., HH > VV. Note that as the grazing angle increases, the contribution of Bragg scattering (the portion of the PSD with Doppler frequencies below ∼60 Hz) also increases. This is due to small scale Bragg scatterers, which are detectable after a wave has broken. The fact that Bragg scatterers appear at both positive and negative Doppler frequencies indicates the effect of orbital motion due to the underlying gravity wave. Orbital motion yields a maximum positive radial velocity for the radar when the Bragg waves are on the crest of the gravity wave and a maximum negative orbital velocity for the radar when the Bragg waves are in the trough of the gravity wave.

F. Breaking-Wave Cross Section

To find the cross section of the breaking wave, we shall adopt a statistical approach, which may at first sight appear to be somewhat qualitative. We argue, however, that this qualitative description is appropriate for several reasons. The first is that "broken" wave surfaces provide the majority contribution to the cross section so that calculations of the scattering of an evolving wave surface before it is "broken" (i.e., considering only the cresting and involution stages during which the assumed two-dimensional (2-D) wave surface is smooth and continuous) address only about 10–20% of the problem. In reality, this approach is also too idealistic because a real breaking wave is decidedly three-dimensional even when generated by 2-D wave drivers, as can be seen in the examples shown in [9]. The second reason is that no two waves break alike and certainly no two broken wave surfaces are alike [9]. Furthermore, present state-of-the-art hydrodynamics lacks the capability to either model or calculate the shape of such convoluted, turbulent surfaces [13], [14]. Thus, detailed scattering calculations from broken wave surfaces, even if such surfaces could be frozen and characterized by a high-speed camera, appear to be infeasible *at present*.

An absolute value of the scattering cross section, however, can be estimated from our measurements. If we review the peak HH RCS levels, which have been measured so far (e.g., Figs. 4 and 5), we notice that they average to a nominal value of HH ∼74 dB. In order to find out what 74 dB corresponds to in RCS, we compare it to calibrations of targets of known cross section. *In situ* calibrations are obtained by backscatter from a 1-in-diameter metal sphere at a range of 10 m and a metal dihedral which is apertured by an opening of 6 in × 6 in size. These results, together with the measured breaking wave cross sections, are tabulated in Table II. In Table II, the first column describes the target, the second column gives the PCR attenuation setting used for the measurement, the third column gives the actual measured relative power level in dB. The fourth column gives the theoretical cross section. For the sphere, since it is in the Mie scattering regime, there is an additional factor f, which for a 1-in ball and a microwave wavenumber of 1.9 cm^{-1} is $f = 1.8$ [15], thus $f\pi r^2 = 9.12 \times 10^{-4}$ m^2, which is shown in the fifth column. For the dihedral, the formula [16] is approximate for the maximum RCS value, which evaluates to 6.22 m^2. However, the measured RCS value of the dihedral referred to the 1-in spherical target is somewhat smaller (by ∼2.6 dB) than the

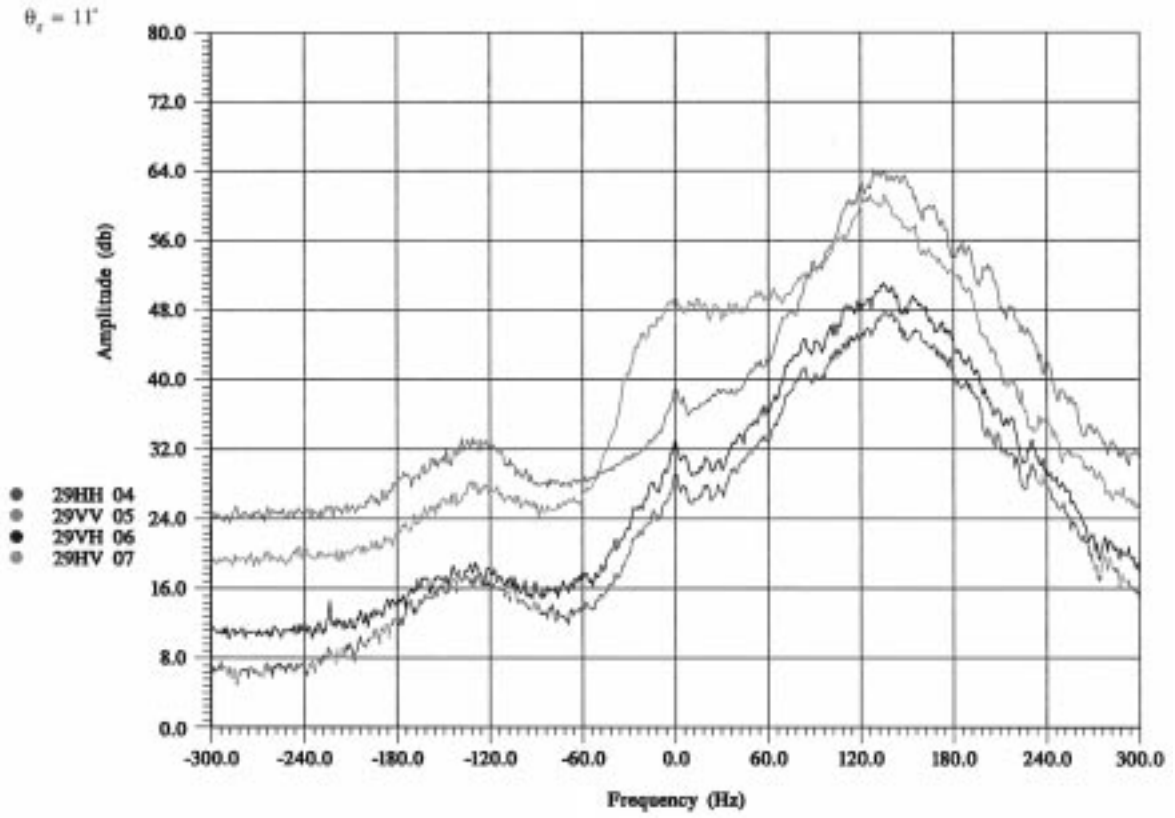

(c)

Fig. 8. (*Continued*.) Examples of Doppler spectra of 4-m sideband-modulated breaking waves. (c) Doppler spectra of HH, VV, VH, and HV from gate 29 at 11° grazing angle. The four different polarizations HH, VV, VH, and HV are represented by the different colors shown on the left side of the figure. Notice that for breaking waves only, the Doppler spectra clearly display the preponderance of super events, i.e., HH > VV. Note that as the grazing angle increases, the contribution of Bragg scattering (the portion of the PSD with Doppler frequencies below ∼60 Hz) also increases. This is due to small scale Bragg scatterers, which are detectable after a wave has broken. The fact that Bragg scatterers appear at both positive and negative Doppler frequencies indicates the effect of orbital motion due to the underlying gravity wave. Orbital motion yields a maximum positive radial velocity for the radar when the Bragg waves are on the crest of the gravity wave and a maximum negative orbital velocity for the radar when the Bragg waves are in the trough of the gravity wave.

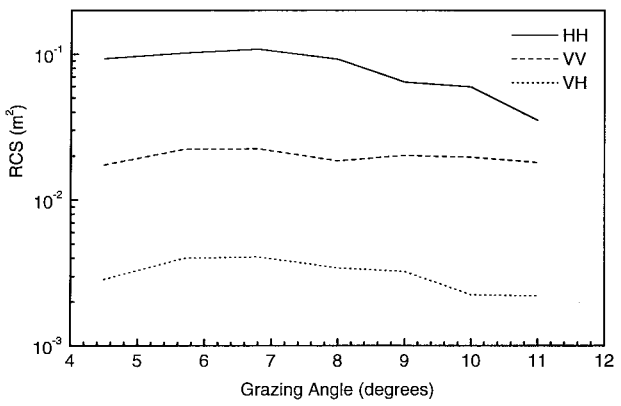

Fig. 9. Breaking-wave radar cross sections versus grazing angle for HH, VV, and VH polarizations (see text for description).

TABLE II
RESULTS OF *IN SITU* CALIBRATION AND CROSS SECTIONS OF VARIOUS "TARGETS" (SEE TEXT FOR DESCRIPTION)

Target	Atten. (dB)	RCS (dB)	$\sigma_{theoretical}$	$\sigma_{theor.}$ [m^2]	$\sigma_{exp.}$ [m^2]
1" sphere	30	54	$f\pi r^2$	$9.12\text{x}10^{-4}$	$9.12\text{x}10^{-4}$
dihedral (6"x6" aperture)	60	60	$\frac{4\pi A^2}{\lambda^2}$	6.22	3.6
Breaking-wave surface	30	HH ~ 74	-	-	$\sim 9\text{x}10^{-2}$

maximum theoretical value. This is probably due to losses through diffraction around the aperture, slight misalignments (i.e., aiming losses) and crudeness of the estimate, etc.

Comparing the ∼74 dB of the breaking wave to the 54 dB of the spherical target, we have

$$\frac{\sigma_{\mathrm{HH}}}{\sigma_{\mathrm{sphere}}} \approx 20 \text{ dB} \tag{3}$$

which yields an HH cross section of

$$\sigma_{\mathrm{HH}} \approx 0.09 \text{ m}^2 \sim 0.1 \text{ m}^2. \tag{4}$$

In other words, this is equivalent to roughly one hundred 1-in-diameter spheres in the range cell, which is 1 m in azimuth by 0.136 m in range. We note that in some cases, spikes appear which are larger than this nominal value by as much as ∼7 dB in which case the $\sigma_{\mathrm{HH}} \approx 0.5 \text{ m}^2$. Using (4) in conjunction with

polarization ratios obtained from Fig. 9 in which the breaking-wave cross sections as a function grazing angle for HH, VV, and VH are plotted, we have

$$\frac{\sigma_{\rm HH}}{\sigma_{\rm VV}} \sim 8 \text{ to } 3 \text{ dB} \tag{5}$$

$$\frac{\sigma_{VH}}{\sigma_{\rm VV}} \sim -8 \text{ to } -10 \text{ dB} \tag{6}$$

for the range of grazing angles of 4.5°–11°.

We note that, in contrast to a point scatterer, the breaking-wave surface is a *distributed scatterer*. Though the unbroken steep crest might be idealized as a line scatterer, nevertheless the broken wave surface generally fills the range cell both in azimuth and in range, which is evident by inspection of the broken wave image (bottom figure) of Fig. 3. Thus, it is appropriate to speak of scatterer density, i.e., σ_o, defined as

$$\sigma^0 = \frac{\sigma}{A_{\rm res}} \tag{7}$$

where $A_{\rm res}$ is the area of the resolution cell. In other words, if the resolution cell size were greater, one would expect to obtain a larger cross section, if the distributed target system uniformly fills the resolution cell. Substituting the value of the RCS from (4) and the value for the range cell area (which in our case is 0.136 m^2) into (7), we obtain $\sigma^0_{\rm HH} \sim 0.7$. This value compares favorably with the value obtained from ocean measurements [17] where a *peak* HH cross section of $\sigma \sim 3.5$ m^2 was measured for a range cell of ∼44 m in azimuthal width (1° beamwidth at 2.5-km range) and 1.5 m in range resolution, giving a sigma-zero value of $\sigma^0_{\rm ocean(HH)} \sim 0.05$. The difference between our measurement and the ocean measurement may be understood in that for our case with a small resolution cell, the breaking-wave surface approximately fills the cell, whereas in the ocean case with a much larger resolution cell (∼66 m^2), one cannot expect the entire area to be filled with broken wave surfaces. Consequently, combining our measurement and the ocean measurement, a fill factor $F = \sigma^0_{\rm ocean(HH)}/\sigma^0_{\rm HH} \sim 7\%$ may be estimated. This indicates that about 7% of the sampled ocean surface is covered by breaking wave surfaces (e.g., white caps, etc.). This number appears to be somewhat high in comparison to a *subjectively* "normal" ocean surface for which only about 1–2% of the surface may be covered by *visible* white-capping breakers. Although the fill factor of incipiently or mildly breaking surfaces might contribute to a substantially higher percentage, it appears that few statistics are available. Two recent papers by Frasier [18] suggest the possibility of providing such statistics using a high-resolution imaging radar.

III. Summary

Using range-resolved measurements and temporal correlations of radar and optical diagnostics we have provided answers to the questions concerning the backscatter from breaking waves, e.g., where does scattering occur? Why is $f_{D(\rm measured)} < f_{D(\rm c-phase)}$? What is the non-Bragg cross section of a breaking wave? We list the main conclusions as follows.

1) In the study of backscatter from vigorously breaking waves (without wind) at small grazing angles, one must bear in mind that the unbroken crest lasts for only a short while and contributes at the beginning of the breaking event. However, the major (∼80–90%) contribution to the fast scatterer cross section comes from the evolving broken crest (or broken wave surface), which is composed of a disordered mass of water, foam, and bubbles.
2) The backscatter from breaking wave surfaces is clearly non-Bragg due to the fact that HH is predominantly greater than VV and that the cross-polarized components are not small. The predominance of HH can be explained by multipath effects and Brewster damping of VV [19].
3) The breaking wave scatterer initially has a speed that exceeds the phase speed of the gravity wave, but then slows down as the wave breaks, ages, and decays. Since the broken-crest contributes to the bulk of the returns and its average speed is slightly less than the phase speed, it follows that the peak PSD frequency, which represents a time average, is less than the Doppler frequency corresponding to the phase speed of the gravity wave.
4) Since no two waves break alike and three-dimensional effects are always present, a statistical description for the characterization of scattering cross section is appropriate. On the average, grazing-angle-dependent measurements in the range of 4.5°–11° indicate that the breaking wave surface is approximately an isotropic scatterer, particularly for VV polarization. Incidentally, scattered visible light (from the OSED illumination) also appears visually to be isotropic over a much larger range of bistatic angles.
5) We have observed in our experiments that mechanically-generated breaking gravity waves produce super events almost exclusively, and we conjecture that at all grazing angles, super events that are also fast scatterers are mainly due to scattering from breaking waves. We would like to point out, however, that we have observed that as the breaking wave becomes less energetic, the time averaged polarization ratio HH/VV also decreases, approaching 0 dB for incipiently breaking waves [5].
6) Since the breaking-wave surface is an efficient depolarizer and super events are predominant, single-bounce mechanisms will not be able to model or reproduce the experimental results so that multibounce scattering appears to be the correct physical scattering mechanism. Furthermore, this multibounce (and/or multipath) scattering must be out-of-plane scattering [6], [12], since in-plane multipath scattering preserves the plane of polarization and does not cause depolarization, i.e., cannot generate cross-polarized returns. Although in-plane multipath scattering can yield a wide range of HH/VV ratios, it cannot produce significant cross-polarized returns.
7) Post-break small scale scatterers are generated by fully breaking gravity waves. Bragg scattering occurs from these small scale scatterers and they are strongly affected by the orbital motion of the underlying gravity wave.
8) For breaking wave surfaces, the nominal measured breaking wave HH backscatter cross section is given

by the empirical result (4) whose value is limited by $\sigma_{\mathrm{X-band}} < 0.5\ \mathrm{m}^2 = -3\ \mathrm{dBm}^2$.

From Fig. 9, the measured "nominal" cross sections are roughly $\sigma_{\mathrm{HH}} \sim 0.1\ \mathrm{m}^2$, $\sigma_{\mathrm{VV}} \sim 0.02\ \mathrm{m}^2$, and $\sigma_{\mathrm{VH}} \sim 0.003\ \mathrm{m}^2$.

ACKNOWLEDGMENT

The authors would like to thank Prof. M. Tulin of OEL/UCSB, Santa Barbara, CA, for the use of his wavetank facility and his staff for providing assistance in the operation of the facility.

REFERENCES

[1] P. H. Y. Lee, J. D. Barter, K. L. Beach, C. L. Hindman, B. M. Lake, H. Rungaldier, J. C. Shelton, A. B. Williams, R. Yee, and H. C. Yuen, "X-band microwave scattering from ocean waves," *J. Geophys. Res.*, vol. 100, pp. 2591–2611, 1995.

[2] P. H. Y. Lee, J. D. Barter, K. L. Beach, E. Caponi, C. L. Hindman, B. M. Lake, H. Rungaldier, and J. C. Shelton, "Power spectral lineshapes of microwave radiation backscattered from sea surfaces at small grazing angles," *Proc. Inst. Elect. Eng.-RSN*, vol. 142, pp. 252–258, 1995.

[3] P. H. Y. Lee, J. D. Barter, E. Caponi, M. Caponi, C. L. Hindman, B. M. Lake, and H. Rungaldier, "Wind-speed dependence of small-grazing-angle microwave backscatter from sea surfaces," *IEEE Trans. Antennas Propagat.*, vol. 44, pp. 333–340, Mar. 1996.

[4] J. D. Barter and P. H. Y. Lee, "Optical polarimetric imaging of scattering surfaces," *Appl. Opt.*, vol. 35, pp. 6015–6027, 1996.

[5] P. H. Y. Lee, J. D. Barter, K. L. Beach, B. M. Lake, H. Rungaldier, J. C. Shelton, H. R. Thompson, Jr., and R. Yee, "Dependence of polarimetric Doppler spectra on breaking-wave energy," in *Proc. Int. Geosci. Remote Sensing Symp.*, Lincoln, NE, May 1996, vol. IV, pp. 2201–2203.

[6] ———, "Depolarization in microwave scatterometry," in *Proc. Int. Geosci. Remote Sensing Symp.*, Lincoln, NE, May 1996, vol. IV, pp. 2213–2215.

[7] P. H. Y. Lee, J. D. Barter, and H. R. Thompson, Jr., "TRW experiments at OEL-UC Santa Barbara—Part 6: Lineshape analysis of breaking-wave spectra," Redondo Beach, CA, TRW Rep. 63817-6001-UT-11.1, Jan. 1996.

[8] P. H. Y. Lee, J. D. Barter, K. L. Beach, C. L. Hindman, B. M. Lake, H. Rungaldier, H. R. Thompson, Jr., and R. Yee, "Experiments on Bragg and non-Bragg scattering using single-frequency and chirped radars," *Radio Sci.*, vol. 32, pp. 1725–1744, 1997.

[9] P. H. Y. Lee and J. D. Barter, "Profiles of breaking gravity waves," Redondo Beach, CA, TRW Rep. 63817-6001-UT-13.1, Aug. 1996.

[10] H. C. Yuen and B. M. Lake, "Nonlinear dynamics of deep-water gravity waves," in *Advances in Applied Mechanics*. New York: Academic, 1982, vol. 22, pp. 68–225.

[11] P. H. Y. Lee, J. D. Barter, K. L. Beach, B. M. Lake, H. Rungaldier, H. R. Thompson, Jr., and R. Yee, "Scattering from breaking waves without wind," Redondo Beach, CA, TRW Rep. 63817-6001-UT-15.4, Mar. 1997.

[12] M. V. Berry, "Interpreting the anholonomy of coiled light," *Nature*, vol. 326, pp. 277–278, 1987.

[13] M. S. Longuet-Higgins, "On the overturning of gravity waves," in *Proc. Royal Soc.*, London, U.K., 1981, vol. A-376, pp. 377–400.

[14] J. C. Lin and D. Rockwell, "Instantaneous structure of a breaking wave," *Phys. Fluids*, vol. 6, pp. 2877–2879, 1994.

[15] G. T. Ruck, D. E. Barrick, W. D. Stuart, and C. K. Krichbaum, *Radar Cross Section Handbook*. New York: Plenum, 1970, vol. 1.

[16] ———, *Radar Cross Section Handbook*. New York: Plenum, 1970, vol. 2.

[17] B. Werle, SMS Inc., Woodland Hills, CA, private communication, 1997.

[18] S. Frasier, "Recent sea spike and ocean surface current measurements obtained with the focused phased array imaging radar (FOPAIR)," presented at *Radar Scattering Ocean Surfaces Meet.*, Santa Barbara, CA, Aug. 1997.

[19] ———, "Current and future directions in field measurements of high-resolution radar scattering," presented at *Radar Scattering Ocean Surfaces Meet.*, Santa Barbara, CA, Aug. 1997.

[20] M. A. Sletten, D. B. Trizna, and J. P. Hansen, "Ultrawide-band radar observations of multipath propagation over the sea surface," *IEEE Trans. Antennas Propagat.*, vol. 44, pp. 646–651, May 1996.

P. H. Y. Lee received the Ph.D. degree in aeronautics (plasma physics) from the California Institute of Technology, Pasadena, in 1973.

From 1973 to 1976, he worked in the Plasma Physics Group and the Fluid Mechanics Department at TRW, Redondo Beach, CA. From 1976 to 1984 he worked at Lawrence Livermore National Laboratory, Livermore, CA, in laser-plasma interactions and laser fusion research. From 1984 to 1991 he worked at Los Alamos National Laboratory, Los Alamos, NM, in subpicosecond intense laser-atom interaction and inductive store-pulsed-power research. He has been at TRW since 1991, investigating the physics of microwave scattering from oceans.

Dr. Lee is an Associate Editor of IEEE TRANSACTIONS ON ANTENNAS AND PROPAGATION.

J. D. Barter received the B.S. degree in physics from Portland State University, OR, in 1968, and the M.S. (physics) and Ph.D. degrees (plasma physics) from the University of Wisconsin, Madison, in 1974 and 1976, respectively.

From 1977 to the present, he has been employed by TRW, Redondo Beach, CA, as a Research Physicist. He participated in plasma physics research from 1977 to 1988 on magnetic confinement devices in the area of ion cyclotron heating. Since 1988 he has been a member of the Ocean Technology Department at TRW and has participated in the study of radar remote sensing of wind roughened surfaces and the development of supporting optical diagnostics.

K. L. Beach received the A.A. degree from Pasadena City College, CA. in 1962.

He has worked for TRW as a Design Engineer since 1966 and has been involved in experimental investigations of rarefied gas dynamics, high-speed wake turbulence, dust lifting during high-explosive events, and water-wave dynamics. He has participated in radar backscatter investigations of wind generated waves in the laboratory and at sea.

B. M. Lake received the B.S.E. degree (honors) from Princeton University, Princeton, NJ, in 1963, and the M.S. and Ph.D. degrees in aeronautics (fluid mechanics) from the California Institute of Technology, Pasadena, in 1964 and 1969, respectively.

He has been with TRW, Redondo Beach, CA, since 1969. He has 28 years of experience in experimental fluid mechanics and the application of instrumentation and sensors to geophysical investigations with particular emphasis on nonacoustic antisubmarine warfare and remote sensing. He has been active not only as a scientific investigator, but also as a technical and business manager. He is a nationally recognized expert on surface-wave hydrodynamics and nonacoustic ASW and has been invited to appear before the House Armed Services Subcommittee as an expert witness on the latter subject.

Dr. Lake is a Technical Fellow of TRW and a Member of the U.S. National Academy of Engineering.

H. Rungaldier received the B.S. degree in mechanical engineering and the M.S. degree in fluid mechanics from the University of California at Berkeley, in 1964 and 1966, respectively.

He has been at TRW, Redondo Beach, CA, for 31 years and has performed experimental investigations of rarefied gas dynamics, high-speed wake turbulence, dust lifting during high-explosive events, low-gravity combustion, and water-wave dynamics. In the latter, he has performed experiments in water-wave evolution and in microwave backscatter investigations of laboratory generated and ocean wind waves.

H. R. Thompson, Jr. received the B.S. degree in physics from Carnegie Mellon University, Pittsburgh, PA, in 1972, and the M.A. (astro-physical sciences) and the Ph.D. degrees (ion cyclotron resonance heating of tokomak plasmas) from Princeton University, Princeton, NJ, in 1977 and 1984, respectively.

From 1984 to 1985, he worked on ion cyclotron resonance heating of magnetic mirrors at the University of California, Irvine. Since 1985 he has been with TRW, Redondo Beach, CA, working on a variety of projects including plasma isotope separation physics, free-electron lasers, super-conducting electron accelerators, and radar remote sensing of water wave surfaces. He has also been involved in the design and construction of state-of-the-art coherent and range-resolved radars.

R. Yee received the A.A. degree in electronics from Los Angeles Technical College, CA, in 1972.

He has worked at TRW, Redondo Beach, CA, for 22 years and has been involved with the design and construction of high-energy lasers, cryo-coolers, and state-of-the-art coherent and range-resolved radars. He has also actively participated in microwave scattering experiments.